

Constraints on the neutron star equation of state from AT2017gfo using radiative transfer simulations

MICHAEL W. COUGHLIN,¹ TIM DIETRICH,² ZOHEYR DOCTOR,^{3,4} DANIEL KASEN,^{5,6} SCOTT COUGHLIN,^{7,8}
ANDERS JERKSTRAND,⁹ GIORGOS LELOUDAS,¹⁰ OWEN MCBRIEN,¹¹ BRIAN D. METZGER,¹² RICHARD O'SHAUGHNESSY,¹³ AND
STEPHEN J. SMARTT¹⁴

¹*Division of Physics, Math, and Astronomy, California Institute of Technology, Pasadena, CA 91125, USA*

²*Nikhef, Science Park 105, 1098 XG Amsterdam, The Netherlands*

³*Kavli Institute for Cosmological Physics, University of Chicago, Chicago, IL 60637, USA*

⁴*Department of Physics, University of Chicago, Chicago, Illinois 60637, USA*

⁵*Departments of Physics and Astronomy, and Theoretical Astrophysics Center, University of California, Berkeley, California 94720-7300, USA*

⁶*Nuclear Science Division, Lawrence Berkeley National Laboratory, Berkeley, California 94720-8169, USA*

⁷*Physics and Astronomy, Cardiff University, Cardiff, CF10 2FH, UK*

⁸*Center for Interdisciplinary Exploration & Research in (CIERA), Northwestern University, Evanston, IL 60208, USA*

⁹*Max-Planck Institut für Astrophysik, Karl-Schwarzschild-Strasse 1, D-85748 Garching, Munich, Germany*

¹⁰*Dark Cosmology Centre, Niels Bohr Institute, University of Copenhagen, Juliane Maries Vej 30, 2100 Copenhagen, Denmark*

¹¹*Astrophysics Research Centre, School of Mathematics and Physics, Queen's University Belfast, Belfast BT7 1NN, Northern Ireland UK*

¹²*Department of Physics and Columbia Astrophysics Laboratory, Columbia University, New York, New York 10027, USA*

¹³*Center for Computational Relativity and Gravitation, Rochester Institute of Technology, Rochester, New York 14623, USA*

¹⁴*Astrophysics Research Centre, School of Mathematics and Physics, Queen's University Belfast, Belfast BT7 1NN, UK*

ABSTRACT

The detection of the binary neutron star merger GW170817 together with the observation of electromagnetic counterparts across the entire spectrum inaugurated a new era of multi-messenger astronomy. In this study we incorporate wavelength-dependent opacities and emissivities calculated from atomic-structure data enabling us to model both the measured lightcurves and spectra of the electromagnetic transient AT2017gfo. Best-fits of the observational data are obtained by Gaussian Process Regression, which allows us to present posterior samples for the kilonova and source properties connected to GW170817. Incorporating constraints obtained from the gravitational wave signal measured by the LIGO-Virgo Scientific Collaboration, we present a 90% upper bound on the mass ratio $q \lesssim 1.38$ and a lower bound on the tidal deformability of $\Lambda \gtrsim 197$, which rules out sufficiently soft equations of state. Our analysis is a path-finder for more realistic kilonova models and shows how the combination of gravitational wave and electromagnetic measurements allow for stringent constraints on the source parameters and the supranuclear equation of state.

Keywords: atomic processes – gravitational waves

INTRODUCTION

A new era of multi-messenger astronomy began with the combined detection of a neutron star (NS) merger via the gravitational wave GW170817 (Abbott et al. 2017a), the gamma-ray burst (GRB) GRB170817A (Abbott et al. 2017b), and the electromagnetic (EM) transient AT2017gfo (Abbott et al. 2017c). The discovery of a bright optical and near-infrared source in NGC4993, consistent with the gravitational-wave sky localization, during the first 12 hrs after the joint gravitational wave and gamma ray detections (Arcavi et al. 2017; Coulter et al. 2017; Lipunov et al. 2017; Soares-Santos et al. 2017; Tanvir et al. 2017; Valenti et al. 2017) led

to intensive follow-up campaigns to show that this was an unusual and unprecedented transient emitting from the X-ray to radio (Alexander et al. 2017; R. Chornock et al. 2017; Cowperthwaite et al. 2017; Drout et al. 2017; Evans et al. 2017; Haggard et al. 2017; Hallinan et al. 2017; Kasliwal et al. 2017; Kilpatrick, C. D. et al. 2017; Margutti et al. 2017; McCully et al. 2017; Nicholl et al. 2017; Shappee et al. 2017; Pian et al. 2017; Smartt et al. 2017; Troja et al. 2017; Utsumi et al. 2017). This event showed that compact binary mergers including at least one NS can create an EM counterpart known as a *kilonova* (Lattimer & Schramm 1974; Li & Paczynski 1998; Metzger et al. 2010; Roberts

et al. 2011; Kasen et al. 2017). Kilonovae originate from neutron-rich outflows from the merger which emit ultraviolet/optical/infrared emission powered by the radioactive decay of r-process elements. Kilonovae are of enormous scientific value: They offer insight into the equation of state (EOS) of NSs (Bauswein et al. 2013a; Abbott et al. 2017a; Radice et al. 2018; Bauswein et al. 2017), the formation of heavy elements (Just et al. 2015; Wu et al. 2016; Roberts et al. 2017; Abbott et al. 2017d), and the expansion rate of the universe (Abbott et al. 2017).

While AT2017gfo is the only confirmed kilonova observed to date, there has been significant theoretical work on modeling the nature of these transients. These studies have postulated two main forms of ejecta from NS mergers: dynamical and wind ejecta. The dynamical ejecta is the matter expelled at the moment of the merger from tidal stripping of the NSs and from the NS-NS contact interface (e.g. Rosswog et al. 1999; Oechslin, R. et al. 2007; Bauswein et al. 2013b; Wanajo et al. 2014; Sekiguchi et al. 2015; Hotokezaka et al. 2016; Rosswog et al. 2017; Wollaeger et al. 2018). Wind ejecta is produced through remnant accretion disk winds, which can be driven by neutrino energy, magnetic fields, viscous evolution and/or nuclear recombination energy (e.g. Fryer et al. 1999; Di Matteo et al. 2002; Metzger et al. 2008; Dessart et al. 2009; Fernández & Metzger 2013; Perego et al. 2014; Siegel et al. 2014; Just et al. 2015; Rezzolla & Kumar 2015; Ciolfi & Siegel 2015; Martinez et al. 2015). The masses, velocities, and compositions of the different ejecta types can vary, which results in different observed kilonova morphology.

The UV - optical - near infrared lightcurves and spectra of AT2017gfo have been used to infer ejecta mass, velocities and compositions when combined with simple toy model approaches (e.g. those of Arnett 1982; Metzger 2017) and more sophisticated modelling of the few existing kilonova simulations, e.g. (Kasen et al. 2017). The first papers published after the event which included quantitative modelling (Cowperthwaite et al. 2017; Kilpatrick, C. D. et al. 2017; Smartt et al. 2017; Tanvir et al. 2017) and later papers based on combined data (Villar et al. 2017; Rosswog et al. 2017; Perego et al. 2017; Waxman et al. 2017a) produced broadly similar results. All the analyses consistently found that a few hundredths of a solar mass was ejected in AT2017gfo at velocities between 0.1 - 0.3 c. However, none of these studies performed fits or inference using full radiative-transfer simulations.

In this work, we build on these previous analyses by performing Bayesian inference on observed AT2017gfo photometry and spectra using “surrogate” models that

are trained on the outputs of radiative transfer simulations. The surrogate models allow one to calculate the likelihood of the data for any ejecta parameters and hence derive posterior distributions on those parameters. Additionally, we go beyond inferences of only ejecta properties and constrain the NS-binary parameters information from full numerical relativity simulations of NS mergers. The contribution of each type of ejecta and their mass, velocity, and composition are expected to depend on the parameters of the compact binary, the compact object masses, spins, orbital eccentricity, as well as the properties of NSs, such as the EOS (Rosswog et al. 1999; Bauswein et al. 2013b; Hotokezaka et al. 2013; Lehner et al. 2016; Radice et al. 2016; Dietrich & Ujevic 2017; Siegel & Metzger 2017; Abbott et al. 2017d). As such, observed kilonova emission can be used to constrain the compact binary parameters (or vice versa) using a mapping from ejecta properties to NS-binary parameters (Coughlin et al. 2017; Abbott et al. 2017). Of particular interest is the EOS of cold supranuclear matter, since it was constrained by the GW170817 signal (Abbott et al. 2017a) and can be independently constrained by the electromagnetic data (Radice et al. 2018).

The layout of this paper is as follows: First, we describe the dataset used for our analysis. Then, we discuss our method for interpolating the output of kilonova simulations over the full parameter space of ejecta mass, velocity, and composition and describe the Bayesian procedure for inferring ejecta properties of AT2017gfo from the photometry. Finally, we use the measured ejecta properties to put new constraints on the NS EOS and the GW170817 binary mass ratio.

DATA

A massive photometric data set was gathered with intra-day time resolution by many teams with latitudinally separated observatories in the southern hemisphere and in Hawaii. We compiled our own selected set of photometry and recalculated bolometric luminosities with realistic error bars. We initially took the photometry from the UV to K -band from (Andreoni et al. 2017; Arcavi et al. 2017; R. Chornock et al. 2017; Cowperthwaite et al. 2017; Drout et al. 2017; Evans et al. 2017; Kasliwal et al. 2017; Tanvir et al. 2017; Pian et al. 2017; Troja et al. 2017; Smartt et al. 2017; Utsumi et al. 2017; Valenti et al. 2017) from phases +0.467d to +25.19d after GW170817 and at each epoch created the broadest spectral energy distribution possible. Data from the Swift satellite in UV bands were only available from Evans et al. (2017) until +1 d and the last U -band detection is from Smartt et al. (2017) at +1.505 d. No se-

cure optical data are available after epoch +11.3 d when AT2017gfo faded below 24 mag in g -band, and the transient is only detected in H and K_s until +14.3 d and then only K_s thereafter.

We began with the photometry of Smartt et al. (2017) as the core data set and employed difference imaging at all epochs of PESSTO (Public ESO Spectroscopic Survey of Transient Objects; Smartt et al. 2015), GROND and Pan-STARRS imaging. Our approach was to: i) complement this photometry only when this was necessary either due to insufficient temporal or wavelength coverage ii) primarily use only *grizyJHK_S* AB mag photometry from sources that used image subtraction (Coward et al. 2017; Andreoni et al. 2017, mostly DECam and Skymapper), or from HST where host contamination is not important (Tanvir et al. 2017) iii) when this was not possible, focus on a small number of independent sources such as Gemini South (Kasliwal et al. 2017), VISTA (Tanvir et al. 2017) and Sirius (Utsumi et al. 2017). We verified consistency between the data sets through direct comparison. In this way, we compiled *grizyJHK_S* SEDs, or as broad a subset as the data allowed. From the first detection at 0.47 d, there are five distinct epochs within the first 24 hrs (including Swift satellite data) at which L_{bol} can be calculated. A total of 20 distinct epochs with enough data to define a black body fit can be defined up to +10.4 d after GW170817. We note that our GROND K -band photometry has been updated compared to Smartt et al. (2017). This is because the GROND template for host subtraction still contained flux from the transient (as first noted by Villar et al. 2017). The image subtraction has now been redone using a different template with no flux present and after this correction, the present GROND light-curve matches much better with other K -band measurements in the literature. The recommended updated photometry values are now published and available on the PESSTO webpage¹ and we employ them here. We used this *ugrizyJHK_S* compilation to constrain the model fits as discussed below.

We have used these data to calculate the bolometric luminosities from +0.467 d to +13.21 d², after which the wavelength coverage is insufficient to securely determine L_{bol} . The bolometric lightcurves are given in Table 2 and their construction in Appendix A. Manual comparison of the models of Kasen et al. (2017) showed some promising agreement with the near infra-red spectrum of R. Chornock et al. (2017) at +2.5 d to +4.5 d

in particular, although only the 1.0-1.8 μm region was compared and the evolution was not consistently reproduced. It is clear that the X-shooter spectra of Pian et al. (2017) and Smartt et al. (2017) taken with ESO's Very Large Telescope contain all available spectral information since they cover 0.35-2.5 μm on a daily basis from +1.5 d to +10.5 d. This is an excellent dataset to more rigorously constrain the ejecta properties. We employed the reduced X-Shooter spectra made publicly available on WISeREP³ and through PESSTO¹. We do not use any other spectral data set, as other data is either inferior signal-to-noise, reduced wavelength coverage, or both, and after +1.5 d, no other spectral dataset provides additional temporal information that enhances the X-shooter sequence in any way.

KILONOVA SURROGATE MODEL

Throughout this work, we use the kilonova models presented in Kasen et al. (2017) which employ a multi-dimensional Monte Carlo code to solve the multi-wavelength radiation transport equation for a relativistically expanding medium. Initial use of the model and comparison to data showed promising similarities with some epochs of near infra-red spectra (R. Chornock et al. 2017) and the bolometric luminosity (Kilpatrick, C. D. et al. 2017). Until now a comparison with the full wavelength and temporal spectral series (X-Shooter spectra from Pian et al. 2017; Smartt et al. 2017) has not been done, but is essential to extract additional details about the ejecta (Smartt et al. 2017; Rosswog et al. 2017; Waxman et al. 2017a). Here we will employ all of the data published to date to constrain the model fits.

The Kasen et al. (2017) models depend parametrically on the ejecta mass M_{ej} , the mass fraction of lanthanides X_{lan} , and the ejecta velocity v_{ej} . In terms of the underlying physics of the merger and ejecta processes described above, these three parameters would be determined by the detailed ejecta processes involved e.g. the duration of the outflow, mass involved, and nucleosynthesis allowed, given the outflow trajectory and neutrino illumination sources. In this work, eschewing detailed neutrino radiation hydrodynamics simulations of mergers, we treat these properties as parameters. We can use separate 1-component models to create a 2-component ejecta model by summing together two 1-component models. This sum is performed by first generating the bolometric lightcurves, photometric lightcurves, and spectra for the individual models. The 2-component bolometric lightcurves and spectra are produced by simply adding the 1-d curves together,

¹ www.pessto.org

² We use the data up to 10 d when calculating the fits.

³ <https://wiserep.weizmann.ac.il>

while the photometric lightcurves are added in the way appropriate for log-based quantities. The use of a 2-component model is motivated by both the theoretical prediction of the presence of different ejecta components and also by the fact that the ejecta are observed to fade rapidly in the UV and optical but have a significantly different near-infrared evolution. We restrict our analysis to spherical symmetry and a uniform composition, and neglect mixing of different ejecta types (Rosswog et al. 2017) when we add the 2 separate model components. The expansion of the model to non-spherical geometries and compositional gradients is left for future analyses.

The model provided in Kasen et al. (2017) and described above is produced on a grid with ejecta masses $M_{\text{ej}}[M_{\odot}] = 0.001, 0.0025, 0.005, 0.0075, 0.01, 0.25, 0.05,$ and 0.1 , ejecta velocities $v_{\text{ej}}[c] = 0.03, 0.05, 0.1, 0.2,$ and 0.3 , and mass fraction of lanthanides $X_{\text{lan}} = 0, 10^{-5}, 10^{-4}, 10^{-3}, 10^{-2},$ and 10^{-1} . The models have temporal epochs of 0.1 day sampling. In order to draw inferences about generic sources not corresponding to one of these gridpoints, we develop a novel method to create a parameterized model from a set of numerical data. We adapt the approach outlined in Doctor et al. (2017) and Pürrer (2014), where Gaussian Process Regression (GPR) is employed to interpolate principal components of gravitational waveforms based on existing sets of simulations. In this analysis, we perform a similar computation but on bolometric luminosities, lightcurves in standard filters, and spectra. The details of the algorithm to perform the interpolation can be found in Appendix B. We also explore in Appendix D the question of whether there are enough simulations on the grid in order to draw inferences based on the model. We show by removing a simulation from the grid and comparing the resulting interpolated lightcurves and spectra to that simulation that the grid is dense enough to reproduce the simulation.

ANALYSIS

We use the Bayesian procedure described in Coughlin et al. (2017) to compare our GPR-based kilonova bolometric, photometric, and spectral models with the full observational data set and draw posterior inferences about our model parameters $v_{\text{ej}}, M_{\text{ej}},$ and X_{lan} . For each component, the flat priors used in our analysis cover the region $-5 \leq \log_{10}(M_{\text{ej}}/M_{\odot}) \leq 0, 0 \leq v_{\text{ej}} \leq 0.3c,$ and $-9 \leq \log_{10}(X_{\text{lan}}) \leq -1$. In all cases, the likelihood is based on the χ^2 value between our model and the data. For the 2-component models, we require $X_{\text{lan}1} > X_{\text{lan}2}$ and $v_1 < v_2$. The velocity prior is employed to limit to systems where the blue ejecta is ahead of the red ejecta,

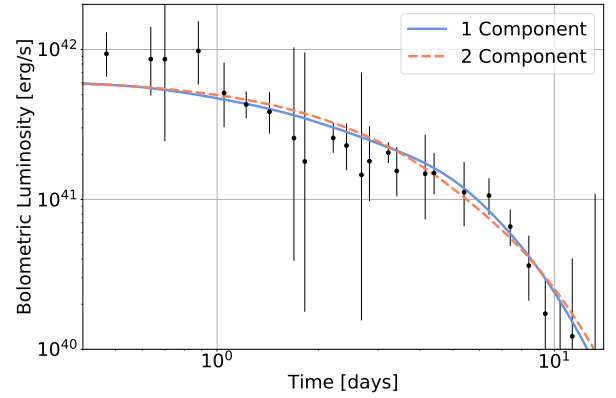


Figure 1. Derived bolometric luminosity and a maximum likelihood χ^2 fit using the 1- and 2-component kilonova bolometric luminosity models of Kasen et al. (2017). We provide the L_{bol} data in Table 2.

which is the regime for this non-interacting model to be valid. The order of the components does reflect their lanthanide fraction, with a large X_{lan} corresponding to a red, lanthanide-rich component and a small X_{lan} to a blue, lanthanide-poor component. In fact, in the one-dimensional picture that we consider here, the blue component cannot be at lower velocity than the red physically because the latter would not allow its emission to escape.

We now discuss this prior choice and the origin of the blue and red component of the kilonovae. In general, there are two options. The first is that the ejecta is to a reasonable approximation isotropic, with a blue component everywhere ahead and faster than the red one. In this case, the present treatment of the multi-component model is appropriate, and all the conclusions derived are consistent. There are reasons to expect this may be the case in certain regimes. First proposed by Metzger & Fernandez (2014), it was thought the only source of the blue ejecta was from the disk wind in the case of a long-lived hypermassive NS and the red ejecta might arise from the tidal tail or a disk wind. The early spectral observations (McCully et al. 2017; Nicholl et al. 2017; Shappee et al. 2017; Smartt et al. 2017) suggest the blue component is moving relatively fast ($\approx 0.3c$) which is likely faster than a standard disk wind would produce, motivating its potential association with dynamical ejecta. This motivates our prior choice.

There is also the possibility that the ejecta is significantly anisotropic or there are significant interactions between different components or with a possible expanding jet. In general, a 2-component model where the components are allowed to interact would be required in this case, although the assumption above is valid in

Table 1. Ejecta properties estimated from the GPR. The estimated uncertainties give the 1σ -uncertainty. Corner plots from which these numbers are derived are shown in Appendix C. The 2 component model lists the higher lanthanide fraction as X_{lan1} and lower as X_{lan2} (corresponding to dynamical and wind components).

	bolometric luminosity		lightcurve		spectra	
	1 component	2 component	1 component	2 component	1 component	2 component
$\log_{10}(M_{\text{ej1}}/M_{\odot})$	$-1.39^{+0.13}_{-0.11}$	$-2.50^{+1.06}_{-1.60}$	$-1.30^{+0.10}_{-0.13}$	$-1.51^{+0.23}_{-0.27}$	$-1.48^{+0.13}_{-0.14}$	$-2.03^{+0.56}_{-1.02}$
$v_{\text{ej1}} [c]$	$+0.12^{+0.09}_{-0.06}$	$+0.09^{+0.09}_{-0.06}$	$+0.23^{+0.06}_{-0.16}$	$+0.10^{+0.08}_{-0.06}$	$+0.20^{+0.003}_{-0.004}$	$+0.10^{+0.08}_{-0.05}$
X_{lan1}	$-6.77^{+1.80}_{-1.30}$	$-2.18^{+1.56}_{-1.16}$	$-3.54^{+0.39}_{-0.36}$	$-1.61^{+0.96}_{-1.04}$	$-2.97^{+0.30}_{-0.39}$	$-1.52^{+0.97}_{-0.98}$
$\log_{10}(M_{\text{ej2}}/M_{\odot})$	–	$-1.39^{+0.13}_{-0.63}$	–	$-1.59^{+0.16}_{-0.18}$	–	$-1.63^{+0.20}_{-0.34}$
$v_{\text{ej2}} [c]$	–	$+0.20^{+0.05}_{-0.08}$	–	$+0.17^{+0.09}_{-0.10}$	–	$+0.20^{+0.03}_{-0.01}$
X_{lan2}	–	$-3.91^{+0.73}_{-0.72}$	–	$-4.73^{+0.41}_{-0.20}$	–	$-3.31^{+0.50}_{-0.77}$

the case that the ejecta is observed from a specific direction such that the lanthanide-free component is ahead of and faster than the red one. The velocity constraints will not be valid if the red and blue components originate from geometrically distinct regions, e.g. if the blue comes out in the polar direction and the red comes out in the equatorial plane. For example, it has been shown that the polar dynamical ejecta could itself be blue (Wanajo et al. 2014; Sekiguchi et al. 2015). In addition, no numerical relativity simulations have produced ejecta masses seen from AT2017gfo ($\approx 0.05M_{\odot}$) in the tidal tail component, while this quantity of red ejecta can readily come from the disk wind in the case that the hypermassive NS is relatively short-lived (Siegel & Metzger 2017). Recently, Kawaguchi et al. (2018) used 2D radiative transfer models to show that the potentially anisotropic properties of the ejecta requires less dynamical and Lanthanide-free ejecta to reproduce AT2017gfo, reducing the tension with numerical relativity simulations. Qualitatively similar results were seen in other studies using 2D models (Wollaeger et al. 2018), and in semi-analytical models that explicitly take into account the non-spherical character of the ejecta (Perego et al. 2017). Another possibility is a 2-component disk wind, e.g. (Shibata et al. 2017). In this case, a fast, blue component is found for the outer torus ejection, and a slow red component for the inner. For this reason, the results derived in the following rely on the assumption that the blue component is everywhere ahead and faster than the red one, which may not be the case.

To validate our analysis procedure, we first reproduce previous bolometric and photometric analyses of this event. The first test is to reproduce the analysis in Smartt et al. (2017), where the bolometric lightcurves were computed from the available photometry at that time. We fit our bolometric models to the bolometric data from Smartt et al. (2017) using a χ^2 likelihood. As shown in Figure 1, both the 1-component and the 2-component model can reproduce the measured bolometric luminosity. Although within error bars, the pre-

dicted bolometric luminosities are systematically low at early times. Based on the 1-component fit to the bolometric luminosity, we estimate $\log_{10}(M_{\text{ej}}) = -1.39$ ($M_{\text{ej}} = 0.041M_{\odot}$), with a velocity of $v_{\text{ej}} = 0.14c$ and a mass fraction of lanthanides of $X_{\text{lan}} = 10^{-6.41}$ (see Table 1 for error bars and Appendix C for the associated corner plots). Overall, this is consistent with Smartt et al. (2017) who found similar ejecta masses and velocities for a composition with an effective gray opacity of $\kappa \sim 0.1 \text{ cm}^2/\text{g}$. Uncertainties in the atomic data render the conversion between opacity and lanthanide mass fraction non-trivial. However previous studies have shown that at $X_{\text{lan}} \sim 10^{-1}$ models have an effective gray opacity of $\kappa \sim 10$, while $X_{\text{lan}} \leq 10^{-6}$ models have an opacity closer to $\kappa \sim 0.1$, with the dependence being roughly logarithmic ($\kappa \propto [\log X_{\text{lan}}]^{\alpha}$). Employing a 2-component model fit to L_{bol} makes a consistent prediction for the light curve and results in a total ejected mass of $M_{\text{ej}} = 0.054M_{\odot}$. While we can measure the total amount of ejecta by using only the bolometric information, the amount of matter in each component (and their composition) is ill-determined; see the top row of the corner plots in Appendix C.

Increasing the complexity of the analyzed data, we fit the broad band photometry points described earlier and illustrated in Figure 2. We assign model uncertainties of 1 mag added in quadrature with the statistical error in the measured photometry (Coughlin et al. 2017). In general, the 1 mag uncertainties, which are treated as 1σ errors, are designed to capture difficult-to-quantify systematic uncertainties, such as those in the the electron fraction and heating rate, which can lead to significant differences in the predicted luminosities (Rosswog et al. 2017). Fitting the lightcurves with a single component results in $\log_{10}(M_{\text{ej}}/M_{\odot}) = -1.41$ ($M_{\text{ej}} = 0.040M_{\odot}$), consistent with our previous findings. However, for early times (< 4 days) the model does not allow a representation of the H -, and K -bands and the predicted g -band is not consistent within the assigned uncertainties after

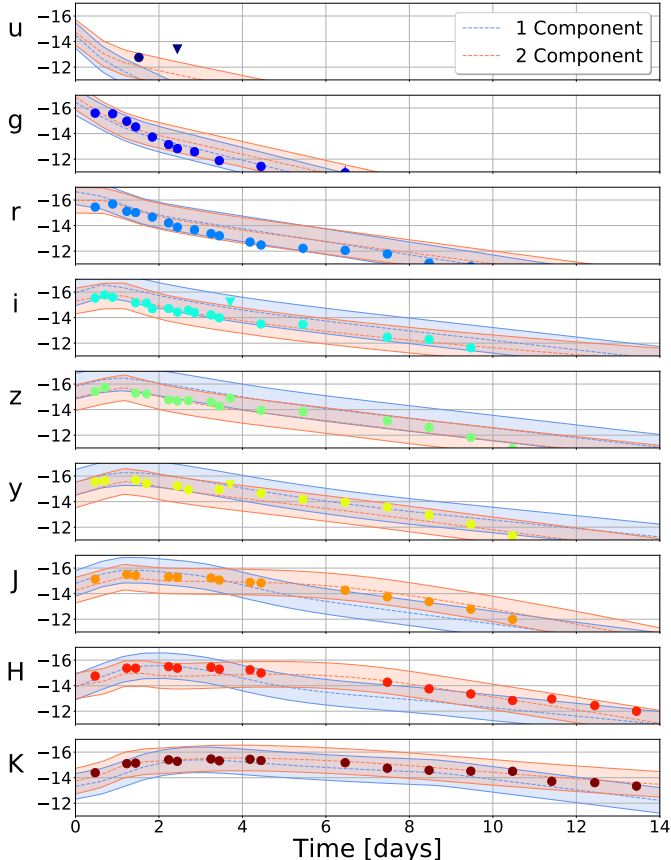


Figure 2. Lightcurves for both one and two component models from Kasen et al. (2017). The shown lightcurves correspond to a maximum likelihood χ^2 fit to the data. Shaded regions represent the assumed 1 mag error budget. The source of the photometry is summarized in Section .

4 days. Conversely, a 2-component model (blue shaded region) can reproduce both early and late-time behavior in all bands. Using photometric data, we can distinguish between the two types of ejecta with different velocities and lanthanide fractions. These two components are not strongly differentiated using bolometric information alone. In our 2-component photometric analysis, we find that the more massive ejecta component has a higher lanthanide fraction. The amount of blue (lanthanide-poor) ejecta is also notable, $\log_{10}(M_{\text{ej}}/M_{\odot}) = -1.59$ ($M_{\text{ej}} = 0.026M_{\odot}$), forming a significant fraction of the total ejecta. We return to the implications for this in the summary.

For the first time, we will also compare the spectra of AT2017gfo against theoretical kilonova predictions to compute posteriors. As discussed in Pian et al. (2017) and Smartt et al. (2017), the first X-Shooter and PESTO EFOSC2 spectra are bright and blue, with rapid cooling just a day later. We fit the spec-

tra of AT2017gfo directly (Pian et al. 2017; Smartt et al. 2017) in figure 3. In line with the uncertainties of the photometric lightcurves, we use an upper error bar of $2.5\times$ the spectral value, and a lower error bar of $1/2.5\times$ the spectral value. This model uncertainty is added in quadrature with the statistical error in the measured spectra. Except for the early epoch when the predicted spectra declines slightly too quickly in the red, broad agreement in the overall shape between the kilonova model and the X-shooter spectra is obtained. Indeed, the model reproduces the spectra within the estimated uncertainty. The fit to the spectra results in $\log_{10}(M_{\text{ej}}/M_{\odot}) = -1.48$ ($M_{\text{ej}} = 0.033M_{\odot}$) for a single component, and $\log_{10}(M_{\text{ej}1}/M_{\odot}) = -2.03$ ($M_{\text{ej}} = 0.010M_{\odot}$), $\log_{10}(M_{\text{ej}2}/M_{\odot}) = -1.63$ ($M_{\text{ej}} = 0.023M_{\odot}$) for the two component model. Overall, we find that the ejecta properties based on the lightcurves and based on the spectra are very similar. This shows that at the level of model uncertainties considered here, for a successful kilonovae model, it is possible to use either the lightcurves or the spectra, but the integrated information of the bolometric luminosity are insufficiently informative to constrain ejecta properties. We show in Appendix D that spectra based on the lightcurve fits (and vice-versa) give reasonable fits as well.

INFERRING SOURCE PROPERTIES

Finally, we want to use our analysis to obtain information about the binary parameters, such as the total mass, mass ratio, and tidal deformability. The idea follows the discussion in Coughlin et al. (2017): namely that information about the ejecta properties can be translated to constraints on the system parameters by fits such as those from Dietrich & Ujevic (2017). In this work, we improve on the fit of Dietrich & Ujevic (2017), which connects the intrinsic binary parameters with dynamical ejecta properties extracted from full 3D numerical relativity simulations. These new fits are described in Appendix E. We emphasize that numerical relativity simulations do not extend significantly past the moment of merger, and so they cannot capture the wind-driven ejecta expected at later times. We therefore for this study assume that the total ejecta mass is parameterized by the total ejected mass given by numerical relativity simulations with a scale factor such that

$$M_{\text{ej}} = A \times M_{\text{ej}}^{\text{NR}} \quad \text{with } A > 1. \quad (1)$$

We sample uniform in A with broad enough priors so as to not affect the posteriors such that we only restrict $A \times M_{\text{ej}}^{\text{NR}}$ to be less than the total mass.

This fit allows us to directly tie the measured ejecta mass and velocity to properties of the binary, includ-

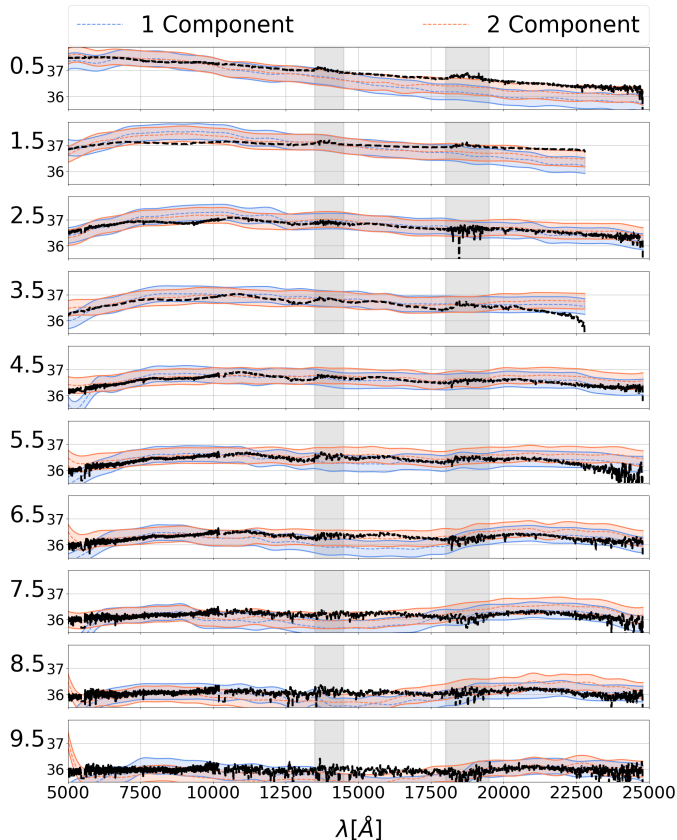


Figure 3. X-shooter spectra (black lines) in units of $\log_{10}(\text{ergs/s}/\text{\AA})$ at the available epochs (in units of days on the far left) and one and two component model fits to the spectra (Pian et al. 2017; Smartt et al. 2017). The shown spectra correspond to a maximum likelihood χ^2 fit to the data. Shaded regions correspond to an assumed 1 mag error budget. The gray shaded regions mark ignored regions due to atmospheric transmission.

ing the mass ratio and equation of state. Based on this fit and the numerical relativity simulations that underly it, the total amount of dynamical ejecta will be largest when the NS involved are less compact. Therefore, based on our estimates for the total amount of ejecta required to explain the kilonova as reported in Table 1, we expect that a self-consistent analysis of EM and GW data will disfavor NSs that are too compact and hence allow us to constrain the nuclear equation of state.

Incorporating information from gravitational-wave parameter estimation, namely a chirp mass M_c of $M_c = 1.188M_\odot$ (Abbott et al. 2017a) and an upper limit on the tidal deformability of $\tilde{\Lambda} \lesssim 640$ ⁴ we are

⁴ The exact value of $\tilde{\Lambda} \lesssim 640$ arises from the fact that as stated in Abbott et al. (2017a) an analysis of GW170817 with the SEOBNRv4_ROM_NRTidal waveform model Bohe et al. (2017);

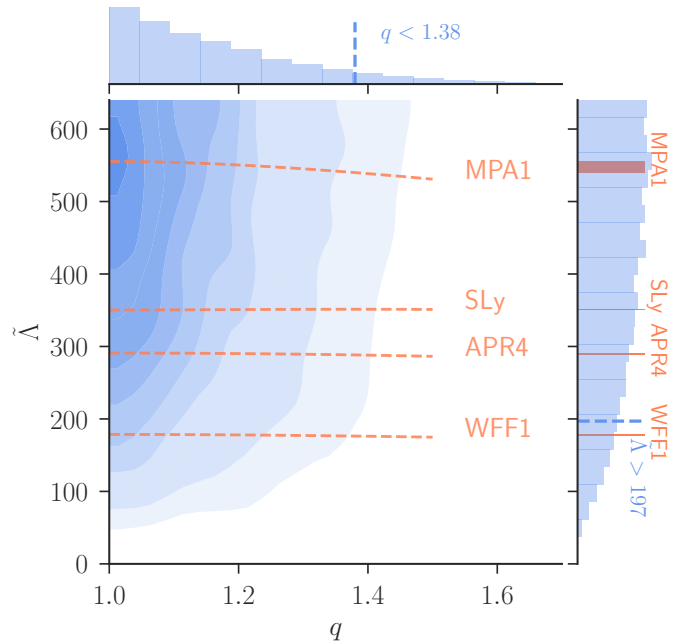


Figure 4. Corner plot for the constraining the mass ratio q , and tidal deformability $\tilde{\Lambda}$ assuming a chirp mass of $M_c = 1.188M_\odot$ and based on the ejecta estimated obtained from the lightcurve fitting. We include estimates for the tidal deformability for a set of possible EOSs as orange lines showing that too soft EOSs are ruled out by our analysis. The numbers represent the 90% limits on the parameters.

able to place constraints on the mass ratio and tidal deformability of the system. Fig. 4 summarizes our findings. We find that the mass ratio of GW170817 is with 90% confidence smaller than $q \lesssim 1.38$, while the 90% lower bound on the tidal deformability is $\tilde{\Lambda} \gtrsim 197$. This lower bound shows that more compact EOSs such as WFF1 are disfavored, see Fig. 4. These results can be compared to estimates obtained from a reanalysis of GW170817 (De et al. 2018), which incorporates quasi-universal relations for the tidal deformability and obtains 90% lower bounds on the tidal deformability $\tilde{\Lambda} \gtrsim 117$ and 90% upper bounds on the mass ratio $q \lesssim 1.51$. Our analysis shows that even without the use of quasi-universal relations tighter constraints on the binary parameters can be obtained from EM observations if bounds on the tidal deformability and the chirp mass can be inferred from GW astronomy. Although broadly consistent, we obtain a more conservative lower bound on the tidal deformability than (Radice et al. 2018), who find lower bounds of $\tilde{\Lambda} \gtrsim 400$ to form disks and ejecta massive enough to create bright EM observ-

Dietrich et al. (2017a, 2018) gives an 80% tighter bound than the PN based TaylorF2 model for which $\tilde{\Lambda} = 800$ was stated.

ables. On the other hand, the radius constraint derived in Bauswein et al. (2017) is in great agreement with our result, since Bauswein et al. (2017) arrive at $\tilde{\Lambda} > 210$. Additionally, also a comparison against Annala et al. (2018) and Most et al. (2018) which obtain, respectively, lower bounds on the tidal deformability of 120 and 375 (2 σ -value) for a 1.4 solar mass NS is possible. Annala et al. (2018) and Most et al. (2018) base their results on constraints obtained from GW170817 and state-of-the-art nuclear physics considerations. While in particular Most et al. (2018) obtains a more stringent bound, very similar to the one of Radice et al. (2018), this result is in agreement with ours since the bound of Most et al. (2018) is based on a large set of possible EOSs and gives credible interval with respect to this comparison set of EOSs and not on the direct measurement of GW170817 or AT2017gfo as done in this work. In addition to q and $\tilde{\Lambda}$, our analysis also allows us to estimate the amount of dynamical ejecta. We find that only 10% of the total amount of ejecta is dynamical ejecta, which supports the idea that the bulk of the ejecta comes from disk outflows (Metzger et al. 2008).

SUMMARY

In this article, we obtained constraints on the GW170817 progenitors mass ratio and tidal deformability, which are more stringent than those obtained purely from gravitational-wave observations. The unknown equation of state can be constrained once information of the observed GW and EM signals are combined. To our knowledge, the presented analysis is the first study constraining the source properties of GW170817 and EOS with statistical methods modeling the lightcurve and spectra of AT2017gfo with surrogate models of radiative transfer simulations, see e.g. Bauswein et al. (2017); Radice et al. (2018) for alternative approaches combining EM and GW information.

Concentrating on the lightcurve fits, given that the broadband colors are the most robustly modeled, a 2-component fit is favored over a 1-component fit, although the single-component fit still broadly reproduces the photometric lightcurves well. The single component fit is consistent with a large ejecta mass $M_{\text{ej}} \approx 0.05M_{\odot}$ and blue (lanthanide-poor) component ($X_{\text{lan}} \approx 3 \times 10^{-4}$). The velocity distribution is broad and slightly bi-modal, partially favoring a low velocity ($v_{\text{ej}} \approx 0.06 c$) and partially a high ($v_{\text{ej}} \approx 0.3 c$).

For the two component fit, our findings of a relatively large ejecta mass $M_{\text{ej}} \approx 0.03M_{\odot}$, and low velocity $v_{\text{ej}} \approx 0.1 c$, for the red (lanthanide-rich) component of the ejecta support its origin as being an outflow from the post-merger accretion disk (Metzger et al.

2008; Fernández & Metzger 2013; Just et al. 2015; Siegel & Metzger 2017), in agreement with previous interpretations of the KN emission from GW170817 (e.g. Cowperthwaite et al. 2017; R. Chornock et al. 2017; Kasen et al. 2017; Villar et al. 2017; Radice et al. 2018). Three-dimensional MHD simulations imply that $\approx 40\%$ of the newly-formed torus can be ejected in winds at typical speeds $v_{\text{ej}} \approx 0.1 c$ (Siegel & Metzger 2017), such that the large inferred ejecta mass for GW170817 is explained by a relatively massive torus, $\approx 0.1 M_{\odot}$. GR simulations show that the latter is a fairly generic outcome of the merger process if the merger remnant first goes through a hypermassive NS phase (e.g. Shibata & Taniguchi 2006), and thus our observations disfavor a prompt collapse (see also Margalit & Metzger 2017; Bauswein et al. 2017). On the other hand, whether the inferred lanthanide mass fraction is sufficient to explain the details of the solar system r -process abundance pattern (which requires $X_{\text{lan}} \approx 0.03 - 0.1$) is less clear; our results depend on the assumption of spherical symmetry, which could overestimate the amount of lanthanide-free ejecta.

By contrast, we infer that the blue (lanthanide-poor) component of the ejecta possesses a somewhat higher velocity $v_{\text{ej}} \gtrsim 0.2 c$ and a similar ejecta mass $M_{\text{ej}} \approx 0.025M_{\odot}$ than the red component. While the velocity scale of the blue ejecta naturally matches expectations for the dynamical ejecta (e.g. Hotokezaka et al. 2013; Bauswein et al. 2013b), the relatively large quantity that we infer appears in tension with current GR merger simulations which focus on dynamical ejection mechanism. This may point to an alternative source of blue ejecta, such as the magnetized neutrino-irradiated wind from a long-lived hypermassive NS remnant prior to its collapse to a black hole (Metzger et al. 2018; a purely neutrino-driven outflow is insufficient to explain the observed properties; Dessart et al. 2009). Alternatively, as with the red ejecta, the blue ejecta could originate from an accretion disk outflow (e.g. Metzger & Fernandez 2014; Perego et al. 2014); however, the high velocity is incompatible with both hydrodynamical and MHD simulations (e.g. Fan et al. 2014; Siegel & Metzger 2017).

Some of the blue light seen at the earliest epoch $\lesssim 1$ day could in principle also be attributed to physical effects not included in our modeling, such as the decay of free neutrons in the outermost fastest parts of the ejecta (Kulkarni 2005; Metzger et al. 2015), or additional thermal energy added to the ejecta by a relativistic jet (“cocoon” emission; Gottlieb et al. 2017; Kasliwal et al. 2017; Piro & Kollmeier 2018), however, see Duffell et al. (2018), who find that relatively little thermal energy is

imparted to the ejecta to power early blue emission in the case of a successful gamma-ray burst jet) or by internal shocks within whatever variable and temporally-extended source (magnetar wind or accretion disk outflow) produces the KN ejecta (Metzger et al. 2018). As already discussed, we cannot exclude that up to $\sim 10\%$ of the ejecta ($\lesssim 6 \times 10^{-3} M_{\odot}$) is dynamical in origin and instead could originate, e.g. from the tidal tail. The tidal tail ejecta is predicted to be fast ($v_{ej} \approx 0.2 - 0.3 c$) and lanthanide-rich ($X_{lan} \gtrsim 0.03$), and its contribution to the light curve may be swamped by other components in the case of NS-NS mergers; prospects are better for unambiguously detecting this component in a NS-BH merger (e.g. Foucart et al. 2017).

Further work is needed due to possible systematic uncertainties introduced by the computation of the ejecta mass in numerical relativity simulations (Dietrich & Ujevic 2017; Coughlin et al. 2017; Abbott et al. 2017d) and the assumptions of our lightcurves as the restriction to spherical geometry. Since opacity and velocity control the diffusion time of the ejecta, the different ejecta channels have different characteristic magnitude, color, and durations. This is further complicated by the fact that the observed color is viewing angle dependent (Kasen et al. 2015) and that dynamical ejecta can have a gravitationally bound component falling back onto the central object, interacting with the outflow and altering the mass ejection and composition of the disk. Fernández et al. (2015) showed that the disk outflow suppresses fallback accretion, and Fernández et al.

(2017) extended this analysis by varying the relative mass ratios of the ejecta by changing the density of the dynamical ejecta. Furthermore, the accuracy of current radiative transfer models in predicting kilonova colors still needs to be fully investigated, and more work is needed to improve atomic line lists, transfer physics, and thermalization (Kasen et al. 2013; Mao et al. 2017; Tanaka 2016). Nevertheless, we have shown how the lightcurve and spectra can be robustly modeled and how parameter estimation pipelines can be employed to determine the source properties from the EM observations.

The lightcurves used in this analysis are publicly available at: https://github.com/dnkasen/Kasen_Kilonova_Models_2017. The lightcurve fitting code is available at: <https://github.com/mcoughlin/gwemlightcurves>.

MC is supported by the David and Ellen Lee Postdoctoral Fellowship at the California Institute of Technology. TD acknowledges support by the European Unions Horizon 2020 research and innovation program under grant agreement No 749145, BNSmergers. ZD is supported by NSF Graduate Research Fellowship grant DGE-1144082. SJS acknowledges funding from STFC grant ST/P000312/1. AJ acknowledges funding by the European Unions Framework Program for Research and Innovation Horizon 2020 under Marie Skłodowska-Curie grant agreement No. 702538. GL is supported by a research grant (19054) from VILLUM FONDEN. ROS is supported by NSF award PHY-1707965.

REFERENCES

- Abbott, B. P., Abbott, R., Abbott, T. D., et al. 2017, *Nature*, 551, 85
- Abbott et al. 2017, *Phys. Rev. Lett.*, 119, 141101. <https://link.aps.org/doi/10.1103/PhysRevLett.119.141101>
- Abbott et al. 2017a, *Phys. Rev. Lett.*, 119, 161101. <https://link.aps.org/doi/10.1103/PhysRevLett.119.161101>
- . 2017b, *The Astrophysical Journal Letters*, 848, L13. <http://stacks.iop.org/2041-8205/848/i=2/a=L13>
- . 2017c, *The Astrophysical Journal Letters*, 848, L12. <http://stacks.iop.org/2041-8205/848/i=2/a=L12>
- . 2017d, *The Astrophysical Journal Letters*, 850, L39. <http://stacks.iop.org/2041-8205/850/i=2/a=L39>
- Alexander, K. D., Berger, E., Fong, W., et al. 2017, *ApJL*, 848, L21
- Andreoni, I., Ackley, K., Cooke, J., et al. 2017, *PASA*, 34, e069
- Annala, E., Gorda, T., Kurkela, A., & Vuorinen, A. 2018, *Phys. Rev. Lett.*, 120, 172703
- Arcavi, I. 2018, *The Astrophysical Journal Letters*, 855, L23. <http://stacks.iop.org/2041-8205/855/i=2/a=L23>
- Arcavi et al. 2017, *Nature*, 551, 64 EP. <http://dx.doi.org/10.1038/nature24291>
- Arnett, W. D. 1982, *ApJ*, 253, 785
- Bauswein, A., Baumgarte, T. W., & Janka, H.-T. 2013a, *Phys. Rev. Lett.*, 111, 131101. <https://link.aps.org/doi/10.1103/PhysRevLett.111.131101>
- Bauswein, A., Goriely, S., & Janka, H.-T. 2013b, *The Astrophysical Journal*, 773, 78. <http://stacks.iop.org/0004-637X/773/i=1/a=78>
- Bauswein et al. 2017, *The Astrophysical Journal Letters*, 850, L34. <http://stacks.iop.org/2041-8205/850/i=2/a=L34>
- Bohe, A., et al. 2017, *Phys. Rev.*, D95, 044028

- Bovard, L., Martin, D., Guercilena, F., et al. 2017, *Phys. Rev.*, D96, 124005
- Ciolfi, R., Kastaun, W., Giacomazzo, B., et al. 2017, *Phys. Rev.*, D95, 063016
- Ciolfi, R., & Siegel, D. M. 2015, *The Astrophysical Journal Letters*, 798, L36.
<http://stacks.iop.org/2041-8205/798/i=2/a=L36>
- Coughlin, M., Dietrich, T., Kawaguchi, K., et al. 2017, *ApJ*, 849, 12
- Coulter, D. A., Foley, R. J., Kilpatrick, C. D., et al. 2017, *Science*, 358, 1556
- Cowperthwaite, P. S., Berger, E., Villar, V. A., et al. 2017, *ApJL*, 848, L17
- De, S., Finstad, D., Lattimer, J. M., et al. 2018, *arXiv:1804.08583*
- Dessart, L., Ott, C., Burrows, A., Rosswog, S., & Livne, E. 2009, *Astrophys. J.*, 690, 1681
- Di Matteo et al. 2002, *The Astrophysical Journal*, 579, 706.
<http://stacks.iop.org/0004-637X/579/i=2/a=706>
- Dietrich, T., Bernuzzi, S., & Tichy, W. 2017a, *Phys. Rev.*, D96, 121501
- Dietrich, T., Bernuzzi, S., Ujevic, M., & Brgmann, B. 2015, *Phys. Rev.*, D91, 124041
- Dietrich, T., & Ujevic, M. 2017, *Class. Quant. Grav.*, 34, 105014
- Dietrich, T., Ujevic, M., Tichy, W., Bernuzzi, S., & Bruegmann, B. 2017b, *Phys. Rev.*, D95, 024029
- Dietrich, T., et al. 2018, *arXiv:1804.02235*
- Doctor, Z., Farr, B., Holz, D. E., & Pürrer, M. 2017, *ArXiv e-prints*, *arXiv:1706.05408*
- Drout, M. R., Piro, A. L., Shappee, B. J., et al. 2017, *Science*, 358, 1570
- Duffell, P. C., Quataert, E., Kasen, D., & Klion, H. 2018, *ArXiv e-prints*, *arXiv:1806.10616*
- Evans, P. A., Cenko, S. B., Kennea, J. A., et al. 2017, *Science*, 358, 1565
- Fan, X., Messenger, C., & Heng, I. S. 2014, *Astrophys. J.*, 795, 43
- Fernández, R., Foucart, F., Kasen, D., et al. 2017, *Classical and Quantum Gravity*, 34, 154001.
<http://stacks.iop.org/0264-9381/34/i=15/a=154001>
- Fernández, R., & Metzger, B. D. 2013, *Monthly Notices of the Royal Astronomical Society*, 435, 502.
[+http://dx.doi.org/10.1093/mnras/stt1312](http://dx.doi.org/10.1093/mnras/stt1312)
- Fernández, R., Quataert, E., Schwab, J., Kasen, D., & Rosswog, S. 2015, *Monthly Notices of the Royal Astronomical Society*, 449, 390.
[+http://dx.doi.org/10.1093/mnras/stv238](http://dx.doi.org/10.1093/mnras/stv238)
- Foreman-Mackey, D. 2016, *JOOS*, 24, [doi:10.21105/joss.00024](https://doi.org/10.21105/joss.00024)
- Foucart, F., Desai, D., Brege, W., et al. 2017, *Classical and Quantum Gravity*, 34, 044002
- Fryer, C. L., Woosley, S. E., & Hartmann, D. H. 1999, *The Astrophysical Journal*, 526, 152.
<http://stacks.iop.org/0004-637X/526/i=1/a=152>
- Gottlieb, O., Nakar, E., Piran, T., & Hotokezaka, K. 2017, *ArXiv e-prints*, *arXiv:1710.05896*
- Haggard, D., Nynka, M., Ruan, J. J., et al. 2017, *ApJL*, 848, L25
- Hallinan, G., Corsi, A., Mooley, K. P., et al. 2017, *Science*, 358, 1579
- Hotokezaka, K., Kiuchi, K., Kyutoku, K., et al. 2013, *Phys. Rev.*, D87, 024001
- Hotokezaka, K., Wanajo, S., Tanaka, M., et al. 2016, *MNRAS*, 459, 35
- Just, O., Bauswein, A., Pulpillo, R. A., Goriely, S., & Janka, H.-T. 2015, *Monthly Notices of the Royal Astronomical Society*, 448, 541.
[+http://dx.doi.org/10.1093/mnras/stv009](http://dx.doi.org/10.1093/mnras/stv009)
- Kasen, D., Badnell, N. R., & Barnes, J. 2013, *Astrophys. J.*, 774, 25
- Kasen, D., Fernandez, R., & Metzger, B. 2015, *Mon. Not. Roy. Astron. Soc.*, 450, 1777
- Kasen, D., Metzger, B., Barnes, J., Quataert, E., & Ramirez-Ruiz, E. 2017, *Nature*, 551, 80 EP .
<http://dx.doi.org/10.1038/nature24453>
- Kasliwal et al. 2017, *Science*, 358, 1559
- Kawaguchi, K., Shibata, M., & Tanaka, M. 2018, *ArXiv e-prints*, *arXiv:1806.04088*
- Kilpatrick, C. D. et al. 2017, *Science*, 358, 1583.
<http://science.sciencemag.org/content/358/6370/1583>
- Kulkarni, S. R. 2005, *ArXiv Astrophysics e-prints*, *astro-ph/0510256*
- Lattimer, J. M., & Schramm, D. N. 1974, *ApJL*, 192, L145
- Lehner, L., Liebling, S. L., Palenzuela, C., et al. 2016, *Classical and Quantum Gravity*, 33, 184002.
<http://stacks.iop.org/0264-9381/33/i=18/a=184002>
- Li, L.-X., & Paczynski, B. 1998, *The Astrophysical Journal Letters*, 507, L59.
<http://stacks.iop.org/1538-4357/507/i=1/a=L59>
- Lipunov et al. 2017, *The Astrophysical Journal Letters*, 850, L1. <http://stacks.iop.org/2041-8205/850/i=1/a=L1>
- Mao, J., Kaastra, J., & Badnell, N. R. 2017, *Astronomy and Astrophysics*, 599, A10
- Margalit, B., & Metzger, B. D. 2017, *The Astrophysical Journal Letters*, 850, L19.
<http://stacks.iop.org/2041-8205/850/i=2/a=L19>
- Margutti, R., Berger, E., Fong, W., et al. 2017, *ApJL*, 848, L20

- Martinez, J. G., Stovall, K., Freire, P. C. C., et al. 2015, *ApJ*, 812, 143
- McCully, C., Hiramatsu, D., Howell, D. A., et al. 2017, *ApJL*, 848, L32
- Metzger, B. D. 2017, *Living Reviews in Relativity*, 20, 3
- Metzger, B. D., Bauswein, A., Goriely, S., & Kasen, D. 2015, *Mon. Not. Roy. Astron. Soc.*, 446, 1115
- Metzger, B. D., & Fernandez, R. 2014, *Monthly Notices of the Royal Astronomical Society*, 441, 3444.
<http://dx.doi.org/10.1093/mnras/stu802>
- Metzger, B. D., Piro, A. L., & Quataert, E. 2008, *Monthly Proceedings of Royal Astronomical Society*, 390, 781
- Metzger, B. D., Thompson, T. A., & Quataert, E. 2018, *The Astrophysical Journal*, 856, 101
- Metzger, B. D., Martínez-Pinedo, G., Darbha, S., et al. 2010, *Monthly Notices of the Royal Astronomical Society*, 406, 2650
- Most, E. R., Weih, L. R., Rezzolla, L., & Schaffner-Bielich, J. 2018, arXiv:1803.00549
- Nicholl et al. 2017, *The Astrophysical Journal Letters*, 848, L18. <http://stacks.iop.org/2041-8205/848/i=2/a=L18>
- Oechslin, R., Janka, H.-T., & Marek, A. 2007, *Astronomy and Astrophysics*, 467, 395.
<https://doi.org/10.1051/0004-6361:20066682>
- Pedregosa, F., Varoquaux, G., Gramfort, A., et al. 2011, *Journal of Machine Learning Research*, 12, 2825
- Perego, A., Radice, D., & Bernuzzi, S. 2017, *Astrophys. J.*, 850, L37
- Perego et al. 2014, *Monthly Notices of the Royal Astronomical Society*, 443, 3134.
[+http://dx.doi.org/10.1093/mnras/stu1352](http://dx.doi.org/10.1093/mnras/stu1352)
- Pian, E., D'Avanzo, P., Benetti, S., et al. 2017, *Nature*, 551, 67
- Pian et al. 2017, *Nature*, 551, 67 EP .
<http://dx.doi.org/10.1038/nature24298>
- Piro, A. L., & Kollmeier, J. A. 2018, *The Astrophysical Journal*, 855, 103
- Pürrer, M. 2014, *Classical and Quantum Gravity*, 31, 195010
- R. Chornock et al. 2017, *The Astrophysical Journal Letters*, 848, L19.
<http://stacks.iop.org/2041-8205/848/i=2/a=L19>
- Radice, D., Galeazzi, F., Lippuner, J., et al. 2016, *Monthly Notices of the Royal Astronomical Society*, 460, 3255.
[+http://dx.doi.org/10.1093/mnras/stw1227](http://dx.doi.org/10.1093/mnras/stw1227)
- Radice, D., Perego, A., Zappa, F., & Bernuzzi, S. 2018, *The Astrophysical Journal Letters*, 852, L29.
<http://stacks.iop.org/2041-8205/852/i=2/a=L29>
- Rasmussen, C. E., & Williams, C. K. I. 2006, *Gaussian Processes for Machine Learning* (MIT Press)
- Rezzolla, L., & Kumar, P. 2015, *Astrophys. J.*, 802, 95
- Roberts, L. F., Kasen, D., Lee, W. H., & Ramirez-Ruiz, E. 2011, *The Astrophysical Journal Letters*, 736, L21.
<http://stacks.iop.org/2041-8205/736/i=1/a=L21>
- Roberts, L. F., Lippuner, J., Duez, M. D., et al. 2017, *Monthly Notices of the Royal Astronomical Society*, 464, 3907. [+http://dx.doi.org/10.1093/mnras/stw2622](http://dx.doi.org/10.1093/mnras/stw2622)
- Rosswog, S., Feindt, U., Korobkin, O., et al. 2017, *Class. Quant. Grav.*, 34, 104001
- Rosswog, S., Liebendörfer, M., Thielemann, F.-K., et al. 1999, *A&A*, 341, 499
- Rosswog, S., Sollerman, J., Feindt, U., et al. 2017, *ArXiv e-prints*, arXiv:1710.05445
- Sekiguchi, Y., Kiuchi, K., Kyutoku, K., & Shibata, M. 2015, *PhRvD*, 91, 064059
- Sekiguchi, Y., Kiuchi, K., Kyutoku, K., Shibata, M., & Taniguchi, K. 2016, *Phys. Rev.*, D93, 124046
- Shappee, B. J., Simon, J. D., Drout, M. R., et al. 2017, *Science*, 358, 1574
- Shibata, M., Fujibayashi, S., Hotokezaka, K., et al. 2017, *Phys. Rev. D*, 96, 123012.
<https://link.aps.org/doi/10.1103/PhysRevD.96.123012>
- Shibata, M., & Taniguchi, K. 2006, *Phys. Rev. D*, 73, 064027.
<https://link.aps.org/doi/10.1103/PhysRevD.73.064027>
- Siegel, D. M., Ciolfi, R., & Rezzolla, L. 2014, *The Astrophysical Journal Letters*, 785, L6.
<http://stacks.iop.org/2041-8205/785/i=1/a=L6>
- Siegel, D. M., & Metzger, B. D. 2017, arXiv:1705.05473
- Smartt, S. J., Valenti, S., Fraser, M., et al. 2015, *A&A*, 579, A40
- Smartt et al. 2017, *Nature*, 551, 75 EP .
<http://dx.doi.org/10.1038/nature24303>
- Soares-Santos et al. 2017, *The Astrophysical Journal Letters*, 848, L16.
<http://stacks.iop.org/2041-8205/848/i=2/a=L16>
- Tanaka, M. 2016, *Adv. Astron.*, 2016, 6341974
- Tanvir et al. 2017, *The Astrophysical Journal Letters*, 848, L27. <http://stacks.iop.org/2041-8205/848/i=2/a=L27>
- Troja, E., Piro, L., van Eerten, H., et al. 2017, *Nature*, 551, 71
- Utsumi, Y., Tanaka, M., Tominaga, N., et al. 2017, *PASJ*, 69, 101
- Valenti et al. 2017, *The Astrophysical Journal Letters*, 848, L24. <http://stacks.iop.org/2041-8205/848/i=2/a=L24>
- Villar, V. A., Guillochon, J., Berger, E., et al. 2017, *The Astrophysical Journal Letters*, 851, L21.
<http://stacks.iop.org/2041-8205/851/i=1/a=L21>

- Wanajo, S., Sekiguchi, Y., Nishimura, N., et al. 2014, *The Astrophysical Journal Letters*, 789, L39.
<http://stacks.iop.org/2041-8205/789/i=2/a=L39>
- Waxman, E., Ofek, E., Kushnir, D., & Gal-Yam, A. 2017a, ArXiv e-prints, arXiv:1711.09638
- . 2017b, ArXiv e-prints, arXiv:1711.09638
- Wollaeger, R. T., Korobkin, O., Fontes, C. J., et al. 2018, *MNRAS*, 478, 3298
- Wu, M.-R., Fernández, R., Martínez-Pinedo, G., & Metzger, B. D. 2016, *Monthly Notices of the Royal Astronomical Society*, 463, 2323.
[+http://dx.doi.org/10.1093/mnras/stw2156](http://dx.doi.org/10.1093/mnras/stw2156)
- Yagi, K., & Yunes, N. 2017, *Phys. Rept.*, 681, 1

APPENDIX

A. LIGHTCURVES

There were some differences in the bolometric luminosity estimated by authors when the first data papers were published on AT2017gfo (see for example [Drout et al. 2017](#); [Smartt et al. 2017](#)) particularly after 9-10 days. [Waxman et al. \(2017b\)](#) have compiled the published data and calculated a bolometric lightcurve and we employ a similar approach here. For example [Smartt et al. \(2017\)](#) only integrated between the observed filter ranges and did not extrapolate beyond $2.5\mu\text{m}$ whereas [Drout et al. \(2017\)](#) and [Waxman et al. \(2017b\)](#) used either a blackbody extrapolation or power law $f(\lambda) \sim \lambda^{-4}$. The real level of emitted flux beyond $2.5\mu\text{m}$ is not constrained by any data available and remains a significant unknown.

We furthermore reconstructed the bolometric light curve for AT2017gfo between +0.47 d and +10.4 d based on these 20 distinct epochs of photometry. In most cases we had sufficient broad band fluxes to construct a black body fit. However, in some cases, we opted to use interpolated photometry to have a data point for missing bands. For example in order to make best use of the early Swift photometry, we have extrapolated ground based optical photometry, but we consider the resulting fit very reasonable. We then fit Planck functions to the multi-wavelength photometry, assuming that the emission can be described by a blackbody. We thus determined the black body temperature and radius and their 68% uncertainties by use of the MATLAB function *fit*. Our estimated bolometric luminosity is therefore the total luminosity emitted at all wavelengths of a black body emitter of that temperature and radius. We have used Monte Carlo resampling to determine the asymmetric errors of the bolometric luminosity. In general, a single blackbody fits satisfactorily up to 5.4 days. It starts to deviate at 6.4, getting worse through 7.4 and 8.4 days and by day 9.4 onwards it is clearly not a single blackbody SED. We therefore consider the bolometric properties determined with this method unreliable past this point in time. Our revised bolometric light curve is provided in Table 2. We have compared our bolometric light curve with those presented by [Waxman et al. \(2017b\)](#) and [Arcavi \(2018\)](#), and we find good agreement in the central values. However, we consider our uncertainties more reasonable, given the assumptions and the photometry errors, while a few points in [Waxman et al. \(2017b\)](#) have unrealistically small uncertainties (below 3%). Our updated L_{bol} values differ from those in [Smartt et al. \(2017\)](#) in particular as that paper only integrated out to the spectral energy distribution out to the red edge of the *K*-band filter.

B. SURROGATE MODEL

The prescription for the algorithm is as follows. First, each bolometric lightcurve, photometric lightcurve, and spectral energy distribution in the simulation set is sparsely interpolated onto the same time array of 0.1 days, which is more densely sampled than most of the data. The bolometric lightcurve and the photometric lightcurves in the various passbands are computed directly from the spectra. For the photometric lightcurves, each passband is analyzed separately and for the spectra, each wavelength is analyzed separately. We denote these vectors of photometry or spectra in one frequency bin for different times as $\tau_i(M_{\text{ej}}^j, v_{\text{ej}}^j, X_{\text{lan}}^j)$ (where i is the i -th time and j is the j -th set of ejecta parameters on the simulation grid) and the matrix of such vectors as $\mathcal{T}_{ij} = [\tau_i(M_{\text{ej}}^j, v_{\text{ej}}^j, X_{\text{lan}}^j)]$. Rather than interpolate the i -th component of τ_i as a function of $(M_{\text{ej}}, v_{\text{ej}}, X_{\text{lan}})$, we instead interpolate principal components of each τ_i vector since entries of τ_i co-vary⁵. Performing a singular value decomposition (SVD) of this matrix

$$\mathcal{T} = V\Sigma U^\top \quad (\text{B1})$$

yields orthonormal basis vectors in the columns and rows of V and U . We then project each τ_i into the left-singular vector basis

$$s_k(M_{\text{ej}}^j, v_{\text{ej}}^j, X_{\text{lan}}^j) = V_{ki}^\top \tau_i(M_{\text{ej}}^j, v_{\text{ej}}^j, X_{\text{lan}}^j) \quad (\text{B2})$$

using all available basis vectors⁶. (Note that Einstein summation notation is used above). This projection results in the s_k components being weights of principal components of the input data \mathcal{T}_{ij} .

We now independently interpolate the k -th component of s_k , conditioning on the known $s_k(M_{\text{ej}}^j, v_{\text{ej}}^j, X_{\text{lan}}^j)$. The interpolation is done using Gaussian process regression (GPR, [Rasmussen & Williams 2006](#)), a statistical interpolation method which produces a posterior distribution on a function f given known values of f at a few points in the

⁵ For simplicity, we ignore the covariance between different frequency bins, which may be included in future analyses.

⁶ The basis is often truncated in many applications to minimize computational resources, but here we keep all basis vectors.

Phase [days]	L [erg/s]	σL^- [erg/s]	σL^+ [erg/s]
0.47	9.4e+41	2.8e+41	3.7e+41
0.64	8.6e+41	3.7e+41	5.5e+41
0.70	8.6e+41	6.2e+41	1.5e+42
0.88	9.8e+41	4.0e+41	5.7e+41
1.05	5.1e+41	2.1e+41	3.0e+41
1.22	4.3e+41	8.1e+40	9.5e+40
1.43	3.8e+41	1.1e+41	1.3e+41
1.69	2.6e+41	2.2e+41	7.8e+41
1.82	1.8e+41	1.6e+41	7.8e+41
2.21	2.6e+41	5.3e+40	6.6e+40
2.42	2.3e+41	7.2e+40	9.2e+40
2.68	1.5e+41	1.3e+41	5.6e+41
2.83	1.8e+41	8.3e+40	1.3e+41
3.22	2.1e+41	3.0e+40	3.6e+40
3.41	1.5e+41	5.0e+40	6.8e+40
4.14	1.5e+41	7.5e+40	1.2e+41
4.40	1.5e+41	4.2e+40	5.5e+40
5.40	1.1e+41	4.5e+40	6.6e+40
6.40	1.1e+41	2.7e+40	3.3e+40
7.40	6.6e+40	1.7e+40	2.0e+40
8.40	3.6e+40	1.5e+40	2.1e+40
9.40	1.7e+40	7.6e+39	1.2e+40
10.40	5.2e+39	4.5e+39	1.6e+40
11.30	1.2e+40	1.0e+40	2.8e+40
13.21	6.8e+39	6.7e+39	1.0e+41

Table 2. Bolometric lightcurve values (and error bars) used in the analysis.

parameter space. Here we describe the basic formulation and facets of Gaussian process regression. We refer the interested reader to [Rasmussen & Williams \(2006\)](#) for a comprehensive and pedagogical description of Gaussian processes. The essential assumption in GPR is that neighboring values of a function $f(\vec{\theta})$ and $f(\vec{\theta}')$ are correlated, and that their joint distribution is a multivariate Gaussian fully described by a mean and covariance. The covariance between function values is prescribed in a kernel function $k(\vec{\theta}, \vec{\theta}')$ that typically depends only on the distance between points $\vec{\theta}$ and $\vec{\theta}'$. A common choice is a Gaussian kernel, for example. To perform a regression, function values \mathbf{f}_* at points Θ_* are inferred by conditioning on known function values after choosing a kernel function. The parameters and/or form of the kernel (called *hyperparameters*), e. g. the Gaussian width, are usually optimized to maximize the evidence for known \mathbf{f} values. Following [Rasmussen & Williams \(2006\)](#) and assuming a zero-mean prior, the posterior distribution on function values \mathbf{f}_* at points Θ_* conditioned on known values \mathbf{f} at Θ has a mean given by

$$K(\Theta_*, \Theta)K(\Theta, \Theta)^{-1}\mathbf{f} \quad (\text{B3})$$

and covariance

$$K(\Theta_*, \Theta_*) - K(\Theta_*, \Theta)K(\Theta, \Theta)^{-1}K(\Theta, \Theta_*) \quad (\text{B4})$$

where the K matrices are the covariance matrices between known and/or inferred function values computed from the kernel. The mean can be used as a simple interpolator, or the full posterior distribution can be used if samples or uncertainties are of interest.

Specifically, we employ the `sci-kit learn` implementation of GPR (Pedregosa et al. 2011). Before interpolation, each s_k is *whitened*:

$$s_k^{\text{whitened}}(M_{\text{ej}}^j, v_{\text{ej}}^j, X_{\text{lan}}^j) = \frac{s_k(M_{\text{ej}}^j, v_{\text{ej}}^j, X_{\text{lan}}^j) - \text{mean}_j \left(s_k(M_{\text{ej}}^j, v_{\text{ej}}^j, X_{\text{lan}}^j) \right)}{\text{range}_j \left(s_k(M_{\text{ej}}^j, v_{\text{ej}}^j, X_{\text{lan}}^j) \right)}. \quad (\text{B5})$$

where “range” indicates the difference of the maximum and minimum values. The mean value of s_k^{whitened} for arbitrary $(M_{\text{ej}}, v_{\text{ej}}, X_{\text{lan}})$ is then regressed with a zero-mean Gaussian process conditioned on $s_k^{\text{whitened}}(M_{\text{ej}}^j, v_{\text{ej}}^j, X_{\text{lan}}^j)$. We assume a rational-quadratic kernel function of the form

$$k(\vec{\theta}, \vec{\theta}') = \left(1 + \frac{|\vec{\theta} - \vec{\theta}'|^2}{2\alpha l^2} \right)^{-\alpha} \quad (\text{B6})$$

where $\vec{\theta}$ and $\vec{\theta}'$ are vectors of input parameters $(M_{\text{ej}}, v_{\text{ej}}, X_{\text{lan}})$. The hyperparameters α and l are chosen by maximizing the evidence for the data under a zero-mean Gaussian process.

The interpolated $s_k^{\text{whitened}}(M_{\text{ej}}, v_{\text{ej}}, X_{\text{lan}})$ is then de-whitened and projected back into the time domain:

$$\tau_i(M_{\text{ej}}, v_{\text{ej}}, X_{\text{lan}}) = V_{ik} s_k(M_{\text{ej}}, v_{\text{ej}}, X_{\text{lan}}) \quad (\text{B7})$$

The interpolated $\tau_i(M_{\text{ej}}, v_{\text{ej}}, X_{\text{lan}})$ is used in computation of the likelihood in the Bayesian inference presented in the next section. The GPR mean is only used here, but future work will incorporate uncertainties from the GPR. We seek to validate the interpolated model using the standard technique of removing the model interpolated at a point ($X_{\text{lan}} = 0.001$, $M_{\text{ej}} = 0.05$, and $v_{\text{ej}} = 0.2$) and comparing the model both with and without its inclusion. Figure 5 shows a comparison of original bolometric luminosity (bottom left), lightcurves (upper left), and spectra (upper right) at this point. The model without the missing point is nearly indistinguishable across the examples here, while the model with the missing point is within error bars of 1 mag assumed in the analysis.

C. CORNER PLOTS

Figure 6 shows the associated “corner” plots (Foreman-Mackey 2016), quantifying the level of overlap between parameters using 1- and 2-D posteriors marginalized over the rest of the parameters.

D. FITS BASED ON THE LIGHTCURVES AND SPECTRA

Figure 7 shows the spectra based on the lightcurve fits (and vice-versa). As explained in the main text we find consistency between fits obtained from the lightcurves or spectra directly.

E. NUMERICAL RELATIVITY FITS

In this article, we improve the fits of Dietrich & Ujevic (2017) to obtain better constraints on the source properties. The two main improvements are that we include a larger set of numerical relativity simulations using results presented in Dietrich et al. (2017b); Hotokezaka et al. (2013); Dietrich et al. (2015); Bauswein et al. (2013b); Lehner et al. (2016); Sekiguchi et al. (2016); Bovard et al. (2017); Shibata et al. (2017); Ciolfi et al. (2017) and that we fit $\log_{10}(M_{\text{ej}})$ instead of M_{ej} . We obtain

$$\log_{10}(M_{\text{ej}}^{\text{NR}}) = \left[\frac{a(1 - 2C_1)M_1}{C_1} + bM_2 \left(\frac{M_1}{M_2} \right)^n + \frac{d}{2} \right] + [1 \leftrightarrow 2] \quad (\text{E8})$$

where $[1 \leftrightarrow 2]$ indicates the sum is repeated with indices switched, with $a = -0.0812$, $b = 0.2288$, $d = -2.16$, $n = -2.51$ and

$$v_{\text{ej}}^{\text{NR}} = \left[\frac{eM_1(fC_1 + 1)}{M_2} + \frac{g}{2} \right] + [1 \leftrightarrow 2] \quad (\text{E9})$$

with $e = -0.3292$, $f = -1.633$, $g = 0.720$, where $M_{1,2}, C_{1,2}$ denote the mass and compactness of the individual stars.

To obtain constraints on the supranuclear equation of state, we rewrite Eqs. (E8) and (E9) to be a function of the tidal deformability

$$\tilde{\Lambda} = \frac{16}{13} \left[\frac{M_1 + 12M_2}{(M_1 + M_2)^5} M_1^4 \tilde{\Lambda}_1 \right] + [1 \leftrightarrow 2]. \quad (\text{E10})$$

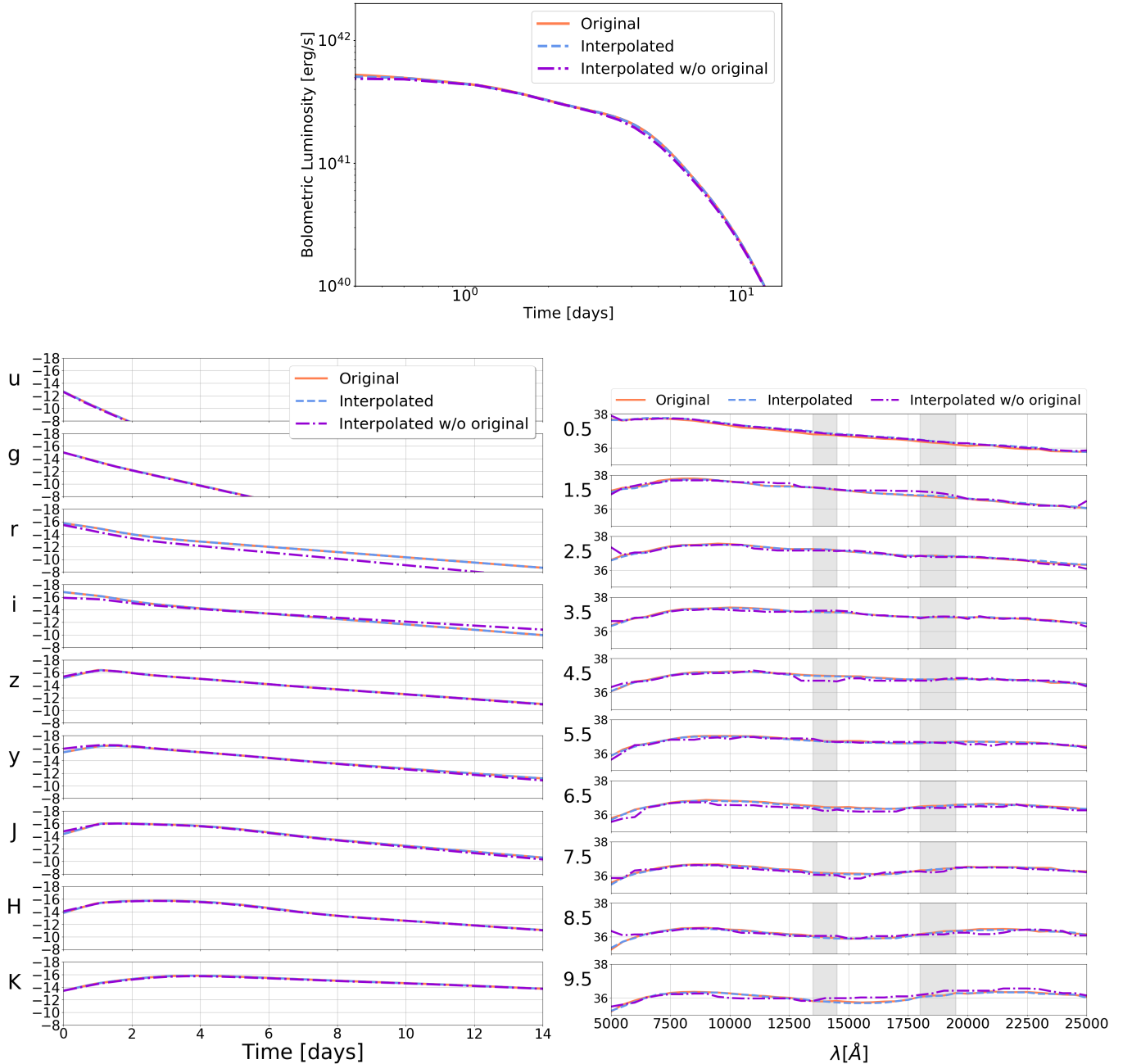


Figure 5. Comparison of original bolometric luminosity (top), lightcurves (bottom left), and spectra (bottom right) with the interpolated model using all points on the grid and an interpolated model with the grid point being tested removed. The grid point tested is $X_{\text{lan}} = 0.001$, $M_{\text{ej}} = 0.05$ and $v_{\text{ej}} = 0.2$.

where $[1 \leftrightarrow 2]$ indicates the sum is repeated with indices switched and $\tilde{\Lambda}_1$ and $\tilde{\Lambda}_2$ are the tidal parameters associated with the individual NSs, and by employing the quasi-universal relations of Yagi & Yunes (2017) and assuming that $M_1/M_2 = C_1/C_2$ which is a valid approximation for realistic masses and compactnesses. We sample uniformly in q and $\tilde{\Lambda}_1$, which uniquely determines $\tilde{\Lambda}$. The constraints on q , $\tilde{\Lambda}$, and A are driven by their predictions for M_{ej} and v_{ej} , in comparison with the measured values from the lightcurve analysis. In general, as either q or $\tilde{\Lambda}$ increases, M_{ej} increases as well.

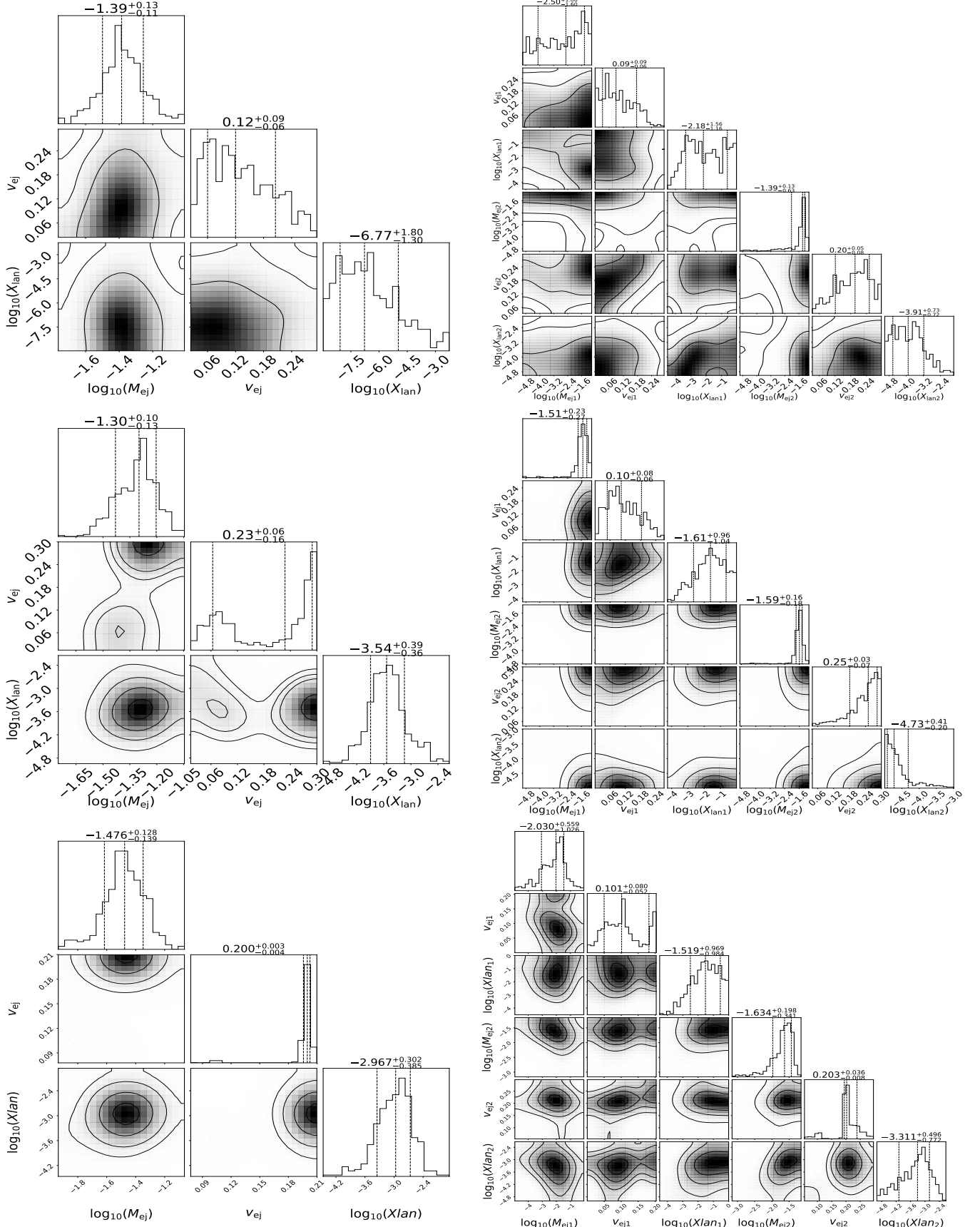


Figure 6. The corner plots for both one (left-column) and two (right-column) component models from Kasen et al. (2017), for the bolometric luminosity (top row), lightcurve (middle row), and spectra (bottom row). The source of the photometry is summarized in section . X-shooter spectra is compiled from Pian et al. (2017) and Smartt et al. (2017).

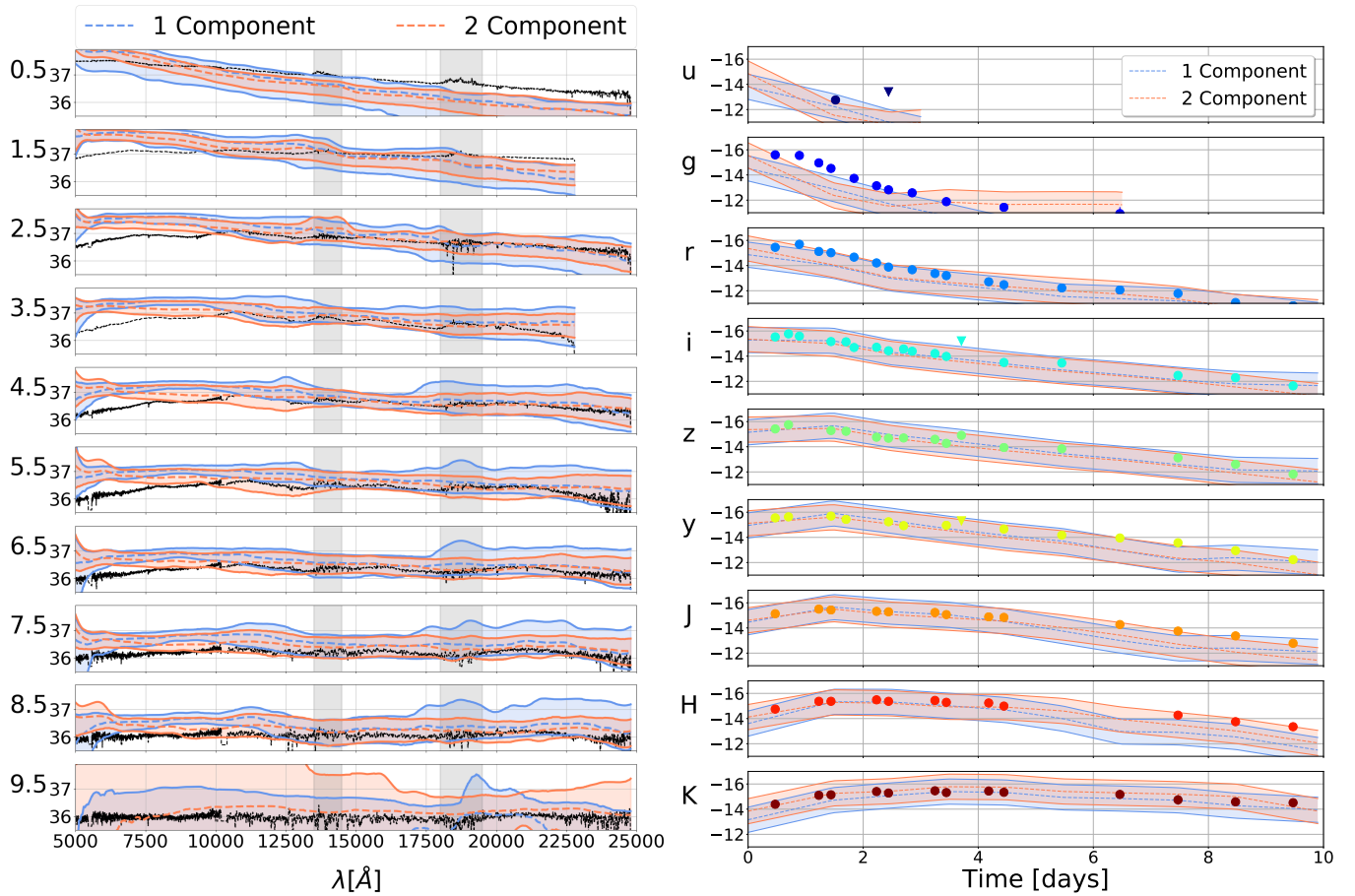


Figure 7. X-shooter spectra (black lines) at the available epochs and one and two component model fits from the lightcurve analysis (Pian et al. 2017; Smartt et al. 2017). The dashed lines show the median spectrum, while the shaded intervals show the 90% intervals. The numbers to the left of the y-axis show the approximate epochs of the observations. The gray vertical shaded regions correspond to parts of the spectrum contaminated by atmospheric transmission. On the right are the photometry with lightcurves derived from the spectra fits.

Note that within our analysis presented in the main text, we do not place any constraints on q from the gravitational-wave analysis. In principle, the posteriors from the gravitational-wave analysis or binary neutron-star population studies could be used to further constrain the distribution of mass ratio or $\tilde{\Lambda}$, but we choose not to do so here. We only impose $M_c = 1.188M_\odot$ and $\tilde{\Lambda} \lesssim 640$ and then employ Eqs. (E8,E9) to determine the mass ratio and tidal deformability of the system and with Eq. (1) to understand how much mass is ejected due to dynamical ejecta mechanism.